Intralanthanide Separation on Layered Titanium(IV) Organophosphate Materials via a Selective Transmetalation Process

Zhang, Wenzhong

2018-07-04

Zhang , W , Hietala , S , Khryashchev , L , Hatanpää , T , Doshi , B & Koivula , R 2018 , ' Intralanthanide Separation on Layered Titanium(IV) Organophosphate Materials via a Selective Transmetalation Process ' , ACS Applied Materials & Interfaces , vol. 10 , no. 26 , pp. 22083-22093 . https://doi.org/10.1021/acsami.8b04480

http://hdl.handle.net/10138/239651
https://doi.org/10.1021/acsami.8b04480

ACS APPLIED MATERIALS & INTERFACES

Research Article

Cite This: ACS Appl. Mater. Interfaces 2018, 10, 22083−22093

www.acsami.org

Intralanthanide Separation on Layered Titanium(IV) Organophosphate Materials via a Selective Transmetalation Process

Wenzhong Zhang,*[,†] Sami Hietala,[‡] Leonid Khriachtchev,[‡] Timo Hatanpää,[‡] Bhairavi Doshi,[§] and Risto Koivula[†]

[†]Department of Chemistry—Radiochemistry and [‡]Department of Chemistry, FI-00014 University of Helsinki, A. I. Virtasen Aukio 1, P. O. Box 55, Helsinki, Finland

[§]Department of Green Chemistry, School of Engineering Science, Lappeenranta University of Technology, Sammonkatu 12, FI-50130 Mikkeli, Finland

Supporting Information

ABSTRACT: The lanthanides (Ln) are an essential part of many advanced technologies. Our societal transformation toward renewable energy drives their ever-growing demand. The similar chemical properties of the Ln pose fundamental difficulties in separating them from each other, yet high purity elements are crucial for specific applications. Here, we propose an intralanthanide separation method utilizing a group of titanium(IV) butyl phosphate coordination polymers as solid-phase extractants. These materials are characterized, and they contain layered structures directed by the hydrophobic interaction of the alkyl chains. The selective Ln uptake results from the transmetalation reaction (framework metal cation exchange), where the titanium(IV) serves as sacrificial coordination centers. The "tetrad effect" is observed from a dilute Ln^{3+} mixture. However, smaller Ln^{3+} ions are preferentially extracted in competitive binary separation models between adjacent Ln pairs. The intralanthanide ion-exchange selectivity arises synergistically from the coordination and steric strain preferences, both of which follow the reversed Ln contraction order. A one-step aqueous separation of neodymium (Nd) and dysprosium (Dy) is quantitatively achievable by simply controlling the solution pH in a batch mode, translating into a separation factor of greater than 2000 and 99.1% molar purity of Dy in the solid phase. Coordination polymers provide a versatile platform for further exploring selective Ln separation processes via the transmetalation process.

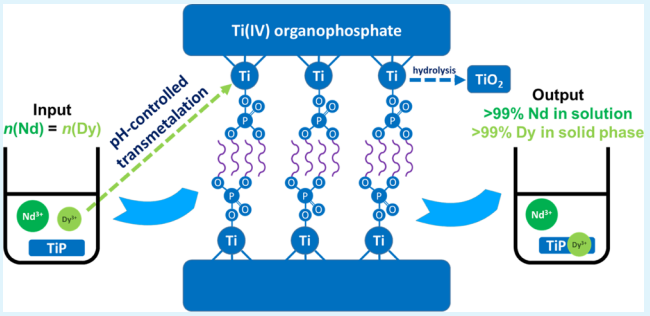

KEYWORDS: *titanium phosphate, ion exchange, lanthanide contraction, organophosphate ligand, solid-phase extraction*

INTRODUCTION

The lanthanide (Ln) series, collectively made up of a group of 15 elements, has gained strategic importance in recent decades. The unique 4f electron structures entail distinctive and, in many cases, irreplaceable physical properties that make Ln essential components in advanced electronics, lasers, and permanent magnets.[1,2] Owing to the poor shielding of nuclear charge by 4f electrons, Ln^{3+} ions share extremely similar yet descending ionic radii across the series with an average difference between adjacent elements of only 1 pm (Ln contraction).[3] Consequently, Ln forms isostructural mineral compounds that are almost always found together in the geosphere.[4] Despite their considerably similar chemical characters, the magnetic and optical properties of Ln differ, and as a result, obtaining pure fractions of individual Ln is crucial for specific applications. The efficient separation of Ln remains a challenging task.

Historically, fraction crystallization was adopted to produce pure Ln.[5] This is proven to be tedious and time-consuming because hundreds of cycles are required. During the Manhattan project, ion-exchange chromatography utilizing organic resins was developed to separate Ln and actinides.[6] The difficulties in continuous operation and resin regeneration restricted its further scalability. Nowadays, continuous liquid−liquid extraction (solvent extraction) is the state-of-the-art technology for Ln separation on an industrial scale.[6] The separation is enabled by complex-forming extractants that selectively transfer the Ln ions from the aqueous to organic phases. Nevertheless, the inevitable liquid waste generation in the solvent extraction process has resulted in a search for more environmentally friendly separation methods.[7]

Recent advances in f-element coordination chemistry have reopened the window for selective crystallization, (bio)-mineralization, and supramolecular self-assembly.[8−14] The small difference in ionic radii can be amplified during the crystallization with desirable multidentate ligands, resulting in

Received: March 19, 2018
Accepted: June 12, 2018
Published: June 12, 2018

Table 1. Formulae and Molecular Mass for TiP Materials

sample	compound formulae	inorganic-to-organic P ratio in synthesis liquor	inorganic-to-organic P ratio in obtained material	molecular mass (g mol^{-1})
TiP_1:0	$TiO_{0.02}(OH)_{2.88}(HPO_4)_{0.23}(H_2PO_4)_{0.62}\cdot 0.25H_2O$	∞	∞	183.9
TiP_3:1	$TiO_{0.43}(OH)_{1.84}(HPO_4)_{0.32}(H_2PO_4)_{0.39}(DBP)_{0.27}\cdot 0.24H_2O$	3	2.63	215.4
TiP_1:1	$TiO_{0.99}(OH)_{0.55}(HPO_4)_{0.24}(H_2PO_4)_{0.28}(DBP)_{0.71}\cdot 0.31H_2O$	1	0.73	277.4
TiP_1:3	$TiO_{1.05}(OH)_{0.13}(HPO_4)_{0.22}(H_2PO_4)_{0.07}(DBP)_{1.26}\cdot 0.10H_2O$	0.33	0.23	360.2
TiP_0:1	$TiO_{1.06}(OH)_{0.01}(H_2PO_4)_{0.24}(DBP)_{1.63}$	0	0.15	429.3

metal−organic framework (MOF) materials with fine-tuned sizes, shapes, and crystal structures.[15] Often, these processes are energy-intensive because they are carried out hydrothermally. Biomineralization is active under milder conditions, yet the stability and reusability of artificial peptides are not satisfactory. Another approach—solid-phase extraction—completely eliminates the organic phase in solvent extraction. Organic−inorganic hybrid materials utilizing an array of inorganic porous supports and organic functional ligands have been developed for selective Ln sorption.[16−20] Recently, we have shown that titanium alkyl-phosphate functionalized mesoporous silica possesses solvating extraction capability.[21] The surface alkyl chains linked to titanium phosphate moieties mimic the structure of tri-*n*-butyl phosphate (TBP) and hence form complexes with Ln nitrates. However, these materials seem not to be perfect candidates for intralanthanide separation because of the similar complex formation constants across the Ln series.

Inorganic ion exchangers, namely, metal(IV) phosphate materials, are used for selective metal separation and decontamination.[17,22,23] Purely inorganic titanium[24] and zirconium phosphate[25] (TiP and ZrP) materials were studied for rare-earth separation via cation exchanges with the proton in the hydrogenphosphate groups. This reversible extraframework cation exchange reaction does not disrupt the building blocks of the material, and therefore the metal selectivity is primarily based on ion-sieve selection and phosphate coordination. Whereas inorganic phosphate offers limited Ln selectivity, simple organic phosphoric acids [e.g., di-*n*-butyl phosphoric acid (HDBP)[26] and di(2-ethylhexyl)-phosphoric acid (DEHPA)[27,28]] demonstrate more promising intralanthanide separation potentials. The ratio of the solubility product constants (K_{sp}) between $Dy(DBP)_3$ and $Nd(DBP)_3$ is reported to be more than 4000 (DBP is the deprotonated form of HDBP).[26] Titanium(IV) forms insoluble, layer-structured precipitates with DBP in the form of a coordination polymer.[29] The resultant material is composed of alternating bilayers of butyl chains and titanium(IV) phosphate. Although titanium(IV) and zirconium(IV) phosphonates were intensively studied,[30,31] there has been extremely limited information regarding the properties and application of titanium(IV) organophosphate materials in metal separation.

In the present work, we describe the synthesis and characterization of layered titanium(IV) butyl phosphate materials and their uptake behavior toward Ln^{3+} ions. Contrary to what we observed from the surface alkyl-phosphate grafted materials, the titanium(IV) butyl phosphate materials do not retain Ln^{3+} in a solvating extraction manner. Instead, the driving force for Ln^{3+} uptake originates from transmetalation reactions [framework Ti(IV) exchange]. Significant group separation was achieved for early and late Ln. This observation forms the basis of a Ln separation strategy that combines both the high selectivity from the crystallization method and the operational convenience from solid-phase extraction.

EXPERIMENTAL SECTION

Chemicals. Titanium(IV) tetrachloride ($TiCl_4$, >97%) and HDBP (>97%) were purchased from Sigma-Aldrich. Lanthanide (including La, Ce, Pr, Nd, Eu, Gd, Tb, Dy, Yb, and Lu) solutions were prepared from their corresponding nitrate salts (>99.9%, Sigma-Aldrich). *ortho*-Phosphoric acid (>99.9%) and ethanol (>99.5%) were purchased from VWR Chemical. For metal (uptake) analysis, elemental standard solutions (1000 mg L^{-1}, PrimAg-plus cert. ref. material) and nitric acid (SpA super purity, 67−69%) were obtained from ROMIL (Cambridge, UK). Ultrapure water (Milli-Q, Millipore) with a resistivity of 18.2 MΩ cm was used.

Synthesis of the TiP Materials. A precipitation method was employed for the synthesis of the TiP materials. By carefully dissolving $TiCl_4$ in water under vigorously stirring (1000 rpm, ∼1 h), a completely transparent Ti(IV) precursor solution (1 M) was obtained. A series of phosphate precursor solutions (0.2 M total P) was prepared by diluting different amounts of 85% H_3PO_4 and HDBP into a 50/50 (v/v) water/ethanol mixture, with the final H_3PO_4-to-HDBP molar ratios at 1:0, 3:1, 1:1, 1:3, and 0:1. The precipitation reaction was carried out by the dropwise addition of 10 mL of the Ti(IV) precursor into 100 mL of the phosphate precursors while stirring (1000 rpm). Note that the P/Ti molar ratio in all synthesis liquors was fixed to 2. The suspension was aged at room temperature for 1 h under the same stirring condition. The resulting white slurry was then washed three times with the water/ethanol mixture through centrifugation (2 min, 5000*g*) and redispersion. Finally, the materials obtained were air-dried at 60 °C in an oven overnight. The materials synthesized from the phosphate precursors with different inorganic-to-organic phosphate ratios were denoted as TiP_*x*/*y*, where *x*/*y* = $n(H_3PO_4)/n(DBP)$ = 1:0, 3:1, 1:1, 1:3, and 0:1 (Table 1). All of them were ground and sieved to a particle size between 74 and 149 μm (100−200 mesh) before further study.

X-ray Diffraction. The powder X-ray diffraction (XRD) patterns in the Bragg−Brentano geometry were recorded by a PANalytical X'Pert3 PW3710 MPD diffractometer control unit, a PW3020 vertical goniometer, and a monochromatic Cu Kα radiation source (λ = 1.54056 Å) operated at 40 kV and 40 mA.

Infrared Spectroscopy. Infrared (IR) spectra (650−4000 cm^{-1}) were recorded on a PerkinElmer Spectrum One Fourier transform infrared (FTIR) spectrometer equipped with a Universal attenuated total reflection (ATR) sampling accessory.

Raman Spectroscopy. Raman spectra were recorded using a confocal Raman microscope (NTEGRA Spectra, NT-MDT) in the 100-to-1200 cm^{-1} region with a spectral resolution of 2 cm^{-1}. The measurements were performed with a 532 nm Nd:YAG laser (output power 20 mW) and a 100× objective. The acquisition time was typically 1 min. We checked that the laser light did not damage the sample.

Surface Area. The Brunauer−Emmett−Teller (BET) surface area and porosity of the materials were determined at 77 K by the nitrogen (N_2) adsorption−desorption method (TriStar II Plus, Micromeritics), and the samples were degassed at 150 °C for 5 h prior to the measurements (VacPrep 061 degassing unit).

Scanning Electron Microscopy. The surface morphology of the TiPs was observed using a Hitachi S-4800 FE-SEM (field-emission

DOI: 10.1021/acsami.8b04480
ACS Appl. Mater. Interfaces 2018, 10, 22083−22093

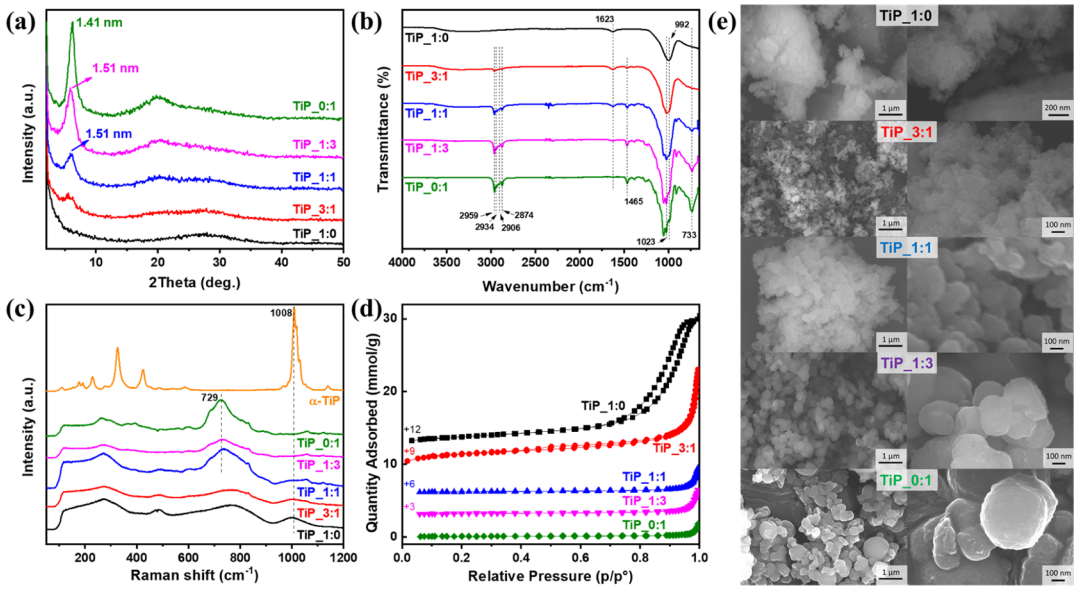

Figure 1. Characterizations of the synthesized TiP materials. (a) Powder XRD patterns. (b) ATR−FTIR spectra. (c) Raman spectra with crystalline α-TiP as a comparison. (d) Nitrogen adsorption−desorption isotherms measured at 77 K. (e) SEM images (smaller magnification in the left column and higher magnification in the right column).

scanning electron microscopy) after they were sputter-coated with a 3 nm layer of Pd−Au alloy.

Compositional Analysis. The elemental contents (C and H) were analyzed using a Thermo Scientific Flash 2000 elemental analyzer. The contents of Ti and P were determined by a PerkinElmer Optima 8300 inductively coupled plasma optical emission spectrometer (ICP-OES) after total digestion in 65% HNO_3 and 1% HF using a CEM MARS 5 microwave digestion system.

Thermogravimetry. The simultaneous thermogravimetry and differential scanning calorimetry−mass spectroscopy (TG/DSC−MS) analysis was performed using a simultaneous TG/DSC apparatus (STA 449F3 Jupiter, Netzsch) connected to a JAS-Agilent GC−MS (7890B GC/MSD5977A). In the dynamic TG measurements, the samples were heated from 30 to 800 °C at a heating rate of 20 °C min^{-1} under a helium gas flow of 40 mL min^{-1}.

Solid-State Nuclear Magnetic Resonance. The solid-state ^{13}C and ^{31}P magic-angle spinning (MAS) nuclear magnetic resonance (NMR) spectra were collected on a Bruker AVANCE III 500 MHz spectrometer equipped with a 4 mm H/X/Y MAS probe. The samples were filled in a 4 mm zirconia rotor and measured at a MAS rate of 12 kHz. ^{13}C spectra were recorded with $^{1}H-^{13}C$ cross-polarization (CP) pulse sequence, 2048 scans, a recycle delay of 5 s, spinal-64 ^{1}H decoupling, and a contact time 0.5 ms. The spectra were referenced with respect to adamantane at 38.5 ppm. ^{31}P spectra were acquired with a 90° pulse (77 kHz rf), a 100 s recycle delay, and 64 scans. The ^{31}P chemical shifts were referred to external 85% H_3PO_4 at 0 ppm.

Metal Concentration Determination. Determination of the metals was performed on an Agilent microwave plasma-atomic emission spectrometer 4200. Depending on suitability, one of Sc, La, or Fe was used as the internal standard for quality control. Samples were diluted to concentrations below 25 mg L^{-1}, and a linear calibration curve was established by 0, 0.5, 1, 2, 5, 10, and 25 mg L^{-1} standard solutions.

Ln^{3+} Uptake Study. The Ln^{3+} ion-exchange extraction was studied in a batch mode. Typically, 50 ± 1 mg of TiP material was placed in a polyethylene vial with 10 mL of Ln^{3+}-containing solution. Samples were equilibrated for 48 h (unless otherwise stated) by constant rotary mixing (50 rpm). The solid/liquid separation was then achieved by filtering through a 0.22 μm poly(vinylidene difluoride) syringe filter, and the clear solution was pipetted for concentration determination. Equilibrium pH was measured from the remaining filtrate.

The distribution coefficient (K_d, mL g^{-1}) demonstrates the distribution of a Ln element (or a group of selected Ln elements) between the solution and the solid material. It was calculated by eq 1:

$$K_d = \frac{[\overline{Ln^{3+}}]_t}{[Ln^{3+}]_t} = \frac{[Ln^{3+}]_i - [Ln^{3+}]_t}{[Ln^{3+}]_t} \times \frac{V}{m} \quad (1)$$

where $[\overline{Ln^{3+}}]_t$ is the Ln^{3+} concentration in the solid (mg g^{-1}) after the sorption, $[Ln^{3+}]_i$ and $[Ln^{3+}]_t$ are, respectively, the Ln^{3+} concentration of the solution before and after sorption (mg L^{-1}), respectively, V is the volume of the solution (10 mL), and m is the mass of the material (0.05 g).

The separation factor (SF) between two Ln^{3+} ions or two groups of Ln^{3+} ions (Ln_1 and Ln_2) was subsequently calculated based on their K_d values (eq 2):

$$SF_{Ln_1/Ln_2} = \frac{K_d(Ln_1)}{K_d(Ln_2)} \quad (2)$$

RESULTS AND DISCUSSION

Synthesis and Characterization of the TiP Materials. $TiCl_4$ is prone to hydrolysis even in acid media, and the stable species of titanium in our synthesis liquor is TiO^{2+} (eq 3), according to the Pourbaix diagram.[32]

$$TiCl_4 + H_2O \rightarrow TiO^{2+} + 2H^+ + 4Cl^- \quad (3)$$

The TiO^{2+} cations are then polymerized to form $(TiO)_n^{2n+}$ chains. Two kinds of phosphate precursors were employed in the synthesis, inorganic *ortho*-phosphoric acid (H_3PO_4) and organic HDBP. Pure inorganic TiPs are a group of $-H_2PO_4$ and/or $-HPO_4$ containing proton-type ion exchangers, which have been extensively studied.[33] The addition of HDBP to the synthesis liquor introduced the butyl phosphate functional groups onto the amorphous TiP assembly based on the inorganic backbone (Ti−O−P) by condensation reactions. In our work, among the TiP materials synthesized (Table 1), TiP_1:0 is a purely inorganic material, whereas TiP_0:1 should supposedly contain only DBP groups. The others are categorized into organic−inorganic mixed TiPs.

DOI: 10.1021/acsami.8b04480
ACS Appl. Mater. Interfaces 2018, 10, 22083−22093

Inorganic TiP_1:0 exhibited a typical amorphous phase with a broad low-intensity powder XRD peak (Figure 1a). The addition of HDBP resulted in the evolution of a peak at 2θ = 5.9−6.3°, which translates into an interlayer spacing of 1.41−1.51 nm. This observation corresponds with an earlier study and suggests that these materials contain self-assembled butyl group layers stacked via van der Waals interactions.[29] Despite the layered structure, the material lacks long-range periodic order. This is mainly due to the high reactivity of Ti(IV), leading to the formation of octahedral Ti-oxo-clusters and consequently amorphous coordination polymers. The high charge and polarizing power of Ti(IV) contribute to the chemical stability of the coordination polymer.[34] A similar situation applies to Zr(IV).[31]

The ATR−FTIR peaks (Figure 1b) centered at 2959, 2934, 2906, and 2874 cm^{-1} are assigned to the stretching vibration of C−H in butyl groups. The 1465 cm^{-1} band represents the deformation vibration of the same groups.[29] The IR absorptions at 1023 and 733 cm^{-1} are typical vibrational modes for C−O−(P) in phase vibration and $P-O_3$ symmetrical stretching, respectively.[35] The water content characterized by the O−H vibration at 1623 cm^{-1} becomes less evident with the increased organic content, as the hydrophobicity increases. The Raman spectra (Figure 1c) revealed additional information regarding the linkage between tetrahedral PO_4 and octahedral TiO_6 groups. The broad peaks at about 730 cm^{-1} in TiP_0:1, TiP_1:3, and TiP_1:1 materials are assigned to the vibration of Ti−O−Ti chains that contain nonbridging oxygen.[36−38] This peak moves toward higher Raman shifts and becomes less evident in TiP_3:1 and TiP_1:0 samples, and it is completely absent in crystalline α-TiP. We therefore infer that the heterocondensation between Ti−O−H and P−O−H groups competes with the homocondensation process for Ti−O−H during the synthesis. HDBP possesses only one P−O−H group, whereas H_3PO_4 harbors three. Because we fixed the overall P/Ti molar ratio at 2, the homocondensation reaction is expected to be more evident in the synthesis precursor with a higher amount of HDBP. In general, the Raman spectra of the TiPs exhibit an amorphous nature without any sharp peaks. The stretching vibrations of the isolated phosphate groups (in the 1000 cm^{-1} region) are only observable from TiPs with a higher inorganic phosphate content (TiP_1:0 and TiP_3:1).

N_2 porosimetry analysis showed that the TiP samples have different textural characteristics, as summarized in Table 2. For the organic-containing TiP materials except TiP_3:1, the N_2 adsorption−desorption isotherms (Figure 1d) are type II with very small hysteresis of type H3, suggesting monolayer−multilayer adsorption and aggregation of particles in these TiP materials. However, TiP_3:1 and purely inorganic TiP_1:0 sample gave a type IV(a) isotherm with a hysteresis in the p/p_0 range of 0.45−1.0 and 0.7−1.0, respectively,[39] which is associated with capillary condensation taking place in their respective mesopores. In TiP_1:0, the hysteresis loop is H2(b), associated with pore blocking, with larger size distribution of the next widths, whereas in TiP_3:1, the change in hysteresis to type H3, due to aggregation of particles. The addition of small amount of organophosphate (in TiP_3:1) increased the surface area and decreased the average particle size (Table 2). As a general trend, the BET surface area decreases drastically with the synthetic addition of organophosphate. The TiP_0:1 sample has a strikingly low surface area (1.2 $m^2\ g^{-1}$), whereas the inorganic amorphous TiP_1:0 sample presents a contrasting value of 142 $m^2\ g^{-1}$. The self-assembly of the butyl groups into a lamellar format resulted in lower pore volume, larger average pore diameter, and significant growth (aggregation) of the particles. This is consistent with the morphological observation by SEM images in Figure 1e. These TiP materials appear as irregular pellets that are connected to each other. It is worth noting that the inorganic TiP_1:0 sample exhibits irregularly shaped large lumps under microscopic observation. The addition of small amount of organophosphate (in TiP_3:1) increased the surface area and decreased the average particle size. The capillary condensation of N_2 shifts to lower relative pressure from the TiP_3:1 to TiP_0:1 sample, reflecting a decrease in the pore volume due to the introduction of organophosphate. The structural and morphological design of the inorganic TiP materials would be beneficial when small amounts of organophosphate are added as structural modifiers. Nevertheless, this is not the target of the current work and would require further and detailed investigation.

Table 2. Textural Parameters of the Synthesized TiPs

sample	S_{BET} (m^2g^{-1})[a]	V_{total} (cm^3g^{-1})[b]	D_{pore} (nm)[c]	$D_{particle}$ (nm)[d]
TiP_1:0	142	0.62	15.1	42.3
TiP_3:1	184	0.43	14.6	32.7
TiP_1:1	16.0	0.12	38.7	375.0
TiP_1:3	6.5	0.05	40.0	916.6
TiP_0:1	1.2	0.01	72.0	5168.2

[a]S_{BET}: BET surface area. [b]V_{total}: total pore volume estimated from the desorption branch by the Barrett−Joyner−Halenda (BJH) method. [c]D_{pore}: average pore diameter estimated from the desorption branch by the BJH method. [d]$D_{particle}$: average particle size calculated by density functional theory.

In order to solve the formulae of the obtained TiP materials, an array of supplementary characterizations was made. The carbon (C), hydrogen (H), titanium (Ti), and phosphorus (P) contents were determined by elemental analysis (EA) and total digestion. The thermogravimetric analysis (TGA) (Figure 2a) weight loss at below 105 °C gave an estimate of the adsorbed water contents (0−3%, Table 3). Solid-state ^{13}C CP MAS NMR (Figure 2b) was run to check that all of the C was sourced from the organic DBP groups and there was no residual solvent. In addition, solid-state ^{31}P MAS NMR with peak deconvolutions (Figure 2c) provided us the relative ratios between the $-H_2PO_4$ and $-HPO_4$ groups. It is reported that peaks with a ^{31}P chemical shift at −5 to −9 ppm result from $-H_2PO_4$ groups, whereas those at −15 to −22 ppm represent $-HPO_4$ groups.[38] Peaks close to 1−2 ppm are assigned to DBP based on our liquid NMR results. The detailed peak positions and relative quantification of the inorganic phosphate groups are present in Table 3. Although the synthesis precursor for TiP_0:1 consisted only of HDBP, inorganic $-H_2PO_4$ groups were found in the final TiP_0:1. For this, a partial hydrolysis of HDBP in acid media would be a logical explanation.

To gain more insights into the composition of the TiP materials, they were calcined at 800 °C under atmospheric condition for 6 h. The resulting white powders were characterized by SEM (Figure S1 in the Supporting Information), XRD, and Raman spectroscopy. The calcined TiP materials are composed of titanium pyrophosphates (Figure 2d), including TiP_2O_7 and $(TiO)_2P_2O_7$ (ICDD card

DOI: 10.1021/acsami.8b04480
ACS Appl. Mater. Interfaces 2018, 10, 22083−22093

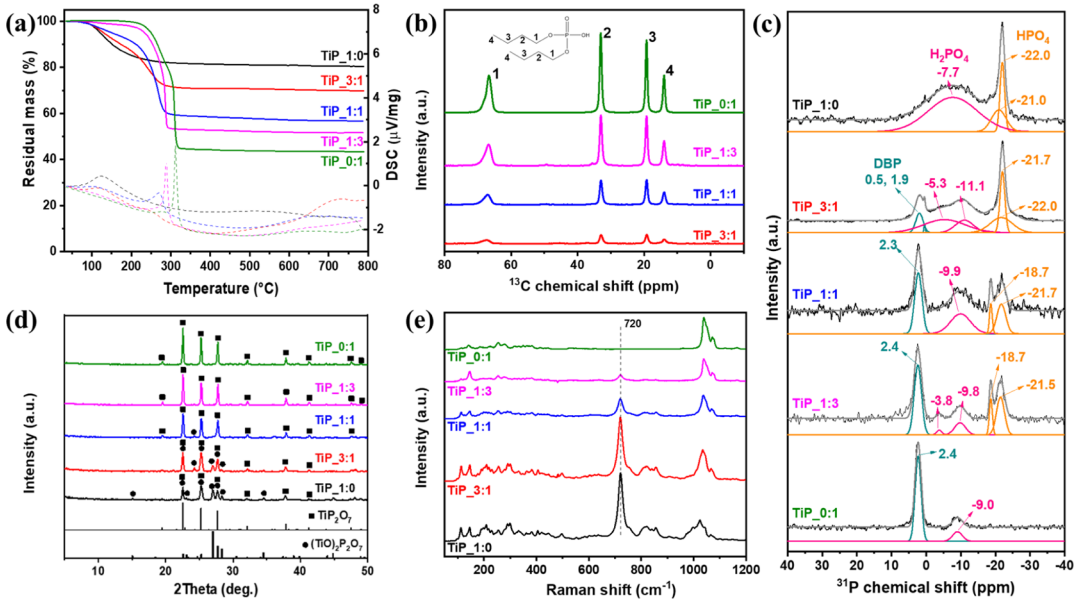

Figure 2. Characterizations in relation to formulae calculations. (a) TG curves (solid line and left *y*-axis) and DSC curves (dashed line and right *y*-axis). (b) ^{13}C CP MAS NMR spectra. (c) ^{31}P MAS NMR spectra with peak deconvolutions. (d) Powder XRD patterns of the calcined TiP materials compared with ICDD reference patterns. (e) Raman spectra of the calcined TiP materials.

Table 3. Characterization Results Used for the Formulae Calculations

					^{31}P NMR peak fitting				TGA		
	EA		digestion		HPO_4		H_2PO_4		DBP	mass loss %	
material	C wt %	H wt %	P wt %	Ti wt %	ppm	%	ppm	%	ppm	105 °C	800 °C
TiP_1:0	0.1	2.8	15.1	27.5	−22.0, −21.0	27.6	−7.7	72.4		2.6	19.6
TiP_3:1	12.7	4.2	15.2	24.0	−22.0, −21.7	45.2	−5.3, −11.1	54.8	0.5, 1.9	2.2	30.1
TiP_1:1	24.5	5.4	13.8	17.3	−21.7, −18.7	46.4	−9.9	53.6	2.3	2.0	43.3
TiP_1:3	33.8	6.5	13.3	13.2	−21.5, −18.7	72.2	−3.8, −9.8	27.8	2.4	0.5	48.3
TiP_0:1	39.0	7.5	14.2	11.9			−9	100	2.3	0.0	56.6

numbers 00-038-1468 and 00-039-0207, respectively). The XRD peaks of these two pyrophosphates overlap to some extent; nevertheless, we were able to distinguish them using Raman spectroscopy. The peak at 720 cm^{-1} (Figure 2e) signifies the presence of Ti−O−Ti chains that contain nonbridging oxygen, as we discussed earlier. Therefore, only $(TiO)_2P_2O_7$ can produce Raman scattering at 720 cm^{-1}. A small amount of amorphous TiO_2 is believed to be present in all calcined samples because of the oxygen-rich calcination environment. Amorphous TiO_2 is a weak Raman scatterer and thus cannot be fully characterized with this technique.[40]

On the basis of all aforementioned characterizations, we were able to determine the composition of the samples. The calculated formulae are listed in Table 1. The detailed calculations and justifications are provided as the Supporting Information. For the TiP materials synthesized from mixed organic−inorganic precursors, the inorganic-to-organic P ratios in the obtained materials are lower than that in the synthesis liquor. Substantially higher Ti(IV) reactivity was observed for HDBP than for H_3PO_4. The obtained titanium(IV) butyl phosphate materials contain hydroxyl and oxy groups. The increased oxy anion content from the TiP_1:0 to TiP_0:1 series confirmed the results from Raman spectroscopy. Solvent extraction of Ti(IV) by DEHPA yields the extractable $[TiO(DEHPA)_2]$ complex, where deprotonated DEHPA acts as a bidentate ligand to occupy the vacant coordination sites of the $(TiO)_n^{2n+}$ chains.[41,42] The TiP_0:1 material is believed to have a similar structure (Scheme 1).

Scheme 1. Proposed Structure of the TiP_0:1 Material Showing the Layered Assembly and the Local Coordination of Ti(IV)

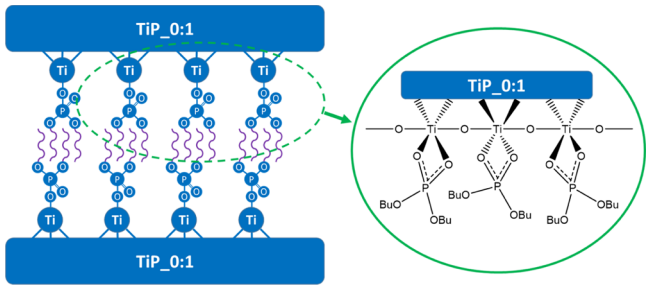

Preliminary Investigation of Ln Uptake Capability. The separation between early and late Ln^{3+} ions serves as a reasonable indicator of the intralanthanide separation capability of the TiP materials. Therefore, preliminary batch trials on competitive Nd−Dy uptake were conducted. The Nd−Dy pair was chosen also because of its industrial relevance with respect to the recycling of NdFeB magnets. In all cases, the total Ln^{3+} uptake increased with the elevated equilibrium pH (Figure S2a) and there were no significant differences in the

DOI: 10.1021/acsami.8b04480
ACS Appl. Mater. Interfaces 2018, 10, 22083−22093

total uptake amounts between the TiP_0:1 and TiP_1:0 samples. However, the SF(Dy/Nd) values for the TiP_1:0 sample stayed between 1 and 2 over the studied pH range (1–3), whereas the same values for TiP_0:1 increased with pH to more than 100 at approximately pH 2.8 (Figure S2b). In the hybrid TiP materials (TiP_1:3, TiP_1:1, and TiP_3:1), the SF(Dy/Nd) maxima were observed in the pH range of 2.2–2.6. The increase of Nd^{3+} uptake after this pH range was responsible for the subsequent decrease in SF(Dy/Nd). The results of the preliminary investigation indicated that TiP_0:1 exhibited the best intralanthanide separation potential. Using the purely inorganic TiP_1:0 as a comparison, the selective uptake of the heavier Ln^{3+} by TiP_0:1 should originate from the effect of the organophosphate functional groups. Therefore, the TiP_0:1 material, prepared from a purely organophosphate precursor, was selected for further separation and mechanism study in the current work. The hybrid TiPs would find applications when the selectivity requirements are not that high or when total Ln uptake is needed.

Proposed Ln^{3+} Uptake Mechanism and Kinetics. Ln^{3+} forms nitrate complexes in aqueous solutions. TBP is a solvating organophosphate extractant that coordinates to neutral $Ln(NO)_3$ complexes (eq 4):

$$Ln^{3+} + 3NO_3^- + 3TBP \leftrightarrow [Ln(NO_3)_3TBP_3] \quad (4)$$

Previously, we reported a group of titanium(IV) alkylphosphate grafted silica materials that retain Ln^{3+} in a solvating extraction manner.[21] The addition of nitrate salts significantly enhanced the uptake of Nd^{3+} and Dy^{3+} on these grafted materials, thereby suggesting that the uptake mechanism follows eq 4. However, the addition of 5 M NH_4NO_3 inhibited the Ln^{3+} uptake on the TiP_0:1 material (Figure S3). To elucidate the uptake mechanism, we closely monitored the Ln^{3+} uptake kinetics in two sorption systems.

The first proposed sorption system I consisted of 2 mM Lu^{3+} at an initial pH of 1.8. The uptake of Lu^{3+} appeared to be relatively slow, reaching less than 30% of the equilibrium uptake after 24 h of mixing (Figure 3a). Notably, significant amounts of Ti (soluble Ti(IV) ions irrespective of speciation) were dissolved into the solution during the first 24 h. The shape of the Ti dissolution amount curve in Figure 3a resembles that of the solution pH changes in Figure 3b. The Lu^{3+} uptake could, therefore, result from the transmetalation reaction: metal cation exchange with framework TiO^{2+}, according to eq 5. Here, the barred ions refer to the solid phase.

$$3\overline{TiO^{2+}} + 2Ln^{3+} \leftrightarrow 2\overline{Ln^{3+}} + 3TiO^{2+} \quad (5)$$

The ratio of dissolved Ti to Lu^{3+} uptake [n(Ti)/n(Lu^{3+})] was calculated and is presented in Figure 3c. The n(Ti)/n(Lu^{3+}) values are always below the theoretical value at 1.5 (according to eq 5) because of the rapid precipitation reaction of TiO^{2+} (eq 6), leading to the decrease in the amount of dissolved Ti, the solution pH, and the n(Ti)/n(Lu^{3+}) value.

$$TiO^{2+} + nH_2O \leftrightarrow TiO(OH)_n^{(2-n)+} + nH^+ \quad (6)$$

The second proposed sorption system II involved competitive Nd^{3+} and Dy^{3+} uptake at an initial pH of 3.6. Over the course of 20 d, the uptake of Nd^{3+} remained negligible (<1 mg g^{-1}) while more than 97% of Dy^{3+} was removed from the solution (Figure 4a). Although the dissolved Ti concentrations were consistently lower than the detection

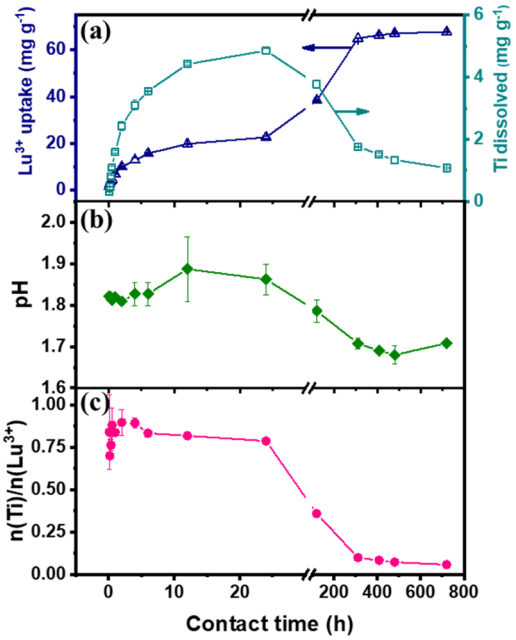

Figure 3. Lu^{3+} uptake kinetics on the TiP_0:1 material (2 mM Lu^{3+}). Effect of contact time on (a) Lu^{3+} uptake and Ti dissolution, (b) solution pH, and (c) n(Ti)/n(Lu^{3+}) ratio.

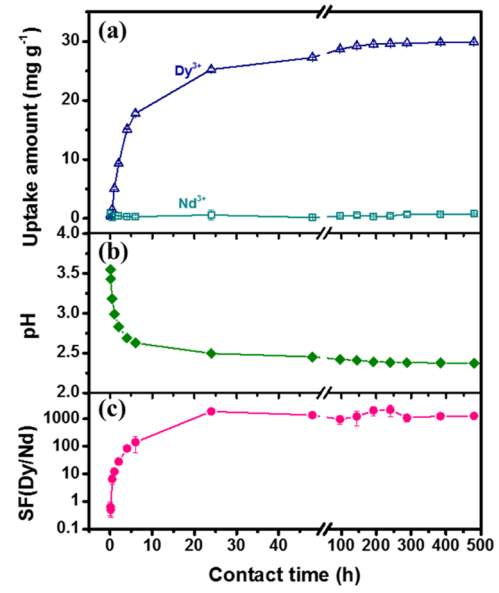

Figure 4. Competitive Nd^{3+} and Dy^{3+} uptake kinetics on the TiP_0:1 material (1 mM equimolar mixture of Nd^{3+} and Dy^{3+}). Effect of contact time on (a) Nd^{3+} and Dy^{3+} uptake, (b) solution pH, and (c) SF(Dy/Nd).

limit (<10 $\mu g\ L^{-1}$), the drastic drop in the solution pH through the initial 10 h of contact (Figure 4b) indicated the ion-exchange dissolution and rapid hydrolysis of TiO^{2+} (faster reaction rate for eq 5 at higher pH). The calculated SFs [SF(Dy/Nd)] reached over 10^3 after 24 h.

The sorption systems I and II were described by common kinetic models, and the detailed results are given in the Supporting Information (Figure S4). On the basis of the obtained high correlation coefficients (R^2 close to 1) and the closeness of the modeled equilibrium uptakes compared with the experimental values, both of the kinetics in systems I and II

DOI: 10.1021/acsami.8b04480
ACS Appl. Mater. Interfaces 2018, 10, 22083–22093

Scheme 2. Proposed Transmetalation Reaction on the TiP_0:1 Material Demonstrating the Exchange of Framework TiO^{2+} with Dy^{3+}

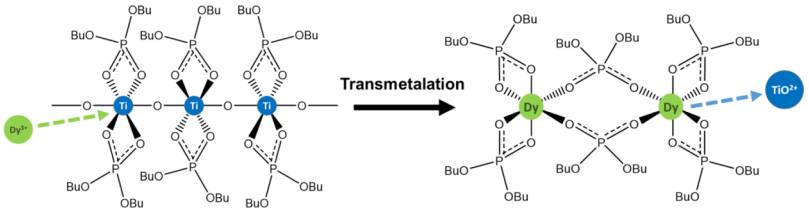

seem to obey the pseudo-second-order model (Table S2). However, further model validation suggested that the errors are not normally distributed and certain points have an unreasonably higher level of influence with a Cook's distance close to 0.5 (Figure S5–S6). The models especially failed to fit the uptake kinetics during the initial 24 h of contact (Figure S7). For system I, the initial accumulation of Ti^{4+} in the solution inhibited the equilibrium in eq 4 from shifting to the right side. For system II, the initial rapid drop in solution pH influenced the reaction rate in eq 5 and the speciation of Dy^{3+} in solution.

When the TiP_0:1 material was equilibrated in 0.1 M HNO_3, a negligible amount of Ti was detected in the solution, thereby excluding the dissolution–precipitation mechanism. Ln^{3+} complexes with dialkylphosphoric acids were determined to be in a polymeric arrangement, in which each Ln^{3+} center is surrounded by six oxygen atoms from the ligand in a pseudo-octahedral environment.[43] Given the above observations, the Ln^{3+} uptake on the TiP_0:1 sample is illustrated in Scheme 2. The selectivity arises from the preferential transmetalation reaction (framework cation exchange). Tasaki-Handa has systematically studied the Ln^{3+}/Ln^{3+} ion-exchange behavior in the coordination polymers based on DEHPA.[44,45] The ion-exchange affinity was ascribed to coordination preference and steric strain. On the one hand, because of the Ln contraction, the coordination preference follows the reverse atomic number sequence in the Ln series. Smaller ions coordinate stronger with the DBP groups. On the other hand, the steric strain effect amplifies the same selectivity order. The ionic radius of Ti^{4+} (74.5 pm) is significantly smaller than that of Ln^{3+} (86.1–103.2 pm, six-coordinated). The non-isostructural insertion of larger Ln^{3+} ions into the TiP framework requires more energy because of the higher degree of structural distortion. The level of steric strain caused by the $TiO^{2+} \leftrightarrow Ln^{3+}$ exchange is expected to be even higher compared to that by the equivalent $Ln^{3+} \leftrightarrow Ln^{3+}$ exchange. Thus, we were able to obtain higher SF(Dy/Nd) values compared with earlier studies using equivalent framework ion exchange[46] and fraction precipitation by organophosphoric acids.[10,26,27]

To support the proposed mechanism, the Dy^{3+}-loaded TiP_0:1 material (after equilibrating for 20 d in system II, denoted as TiP_0:1_Dy) was characterized and compared with pristine TiP_0:1 as well as the synthesized pure $Dy(DBP)_3$ and/or $Nd(DBP)_3$ coordination polymers. Powder XRD patterns (Figure 5a) reveal the shrinkage of interlayer distance after Dy^{3+} exchange and structural distortion. Two peaks appeared for the TiP_0:1_Dy sample corresponding to *d* spacings of 1.40 and 1.31 nm. $Dy(DBP)_3$ crystallizes in a monoclinic fashion,[26] and the peak (d = 1.29 nm) here represents the distance between the chains. The ATR–FTIR spectra (Figure 5b) show a doublet at approximately 1170 and 1100 cm^{-1}, supposedly because of the vibration of the POO^- group.[44] This exact doublet shifted toward the value of $Dy(DBP)_3$ in the TiP_0:1_Dy sample. The Raman and UV–vis diffuse reflectance spectra were also checked before and after Dy^{3+} loading, yet no evident changes were found. Hydrolysis induced small amounts of $-H_2PO_4$ groups, as they were found by the ^{31}P NMR peaks with chemical shifts at −18.4 and −21.4 ppm in the TiP_0:1_Dy material (Figure 5c). Further studies in exploring the local coordination environment of the loaded Ln^{3+} are needed to fully justify our proposed mechanism.

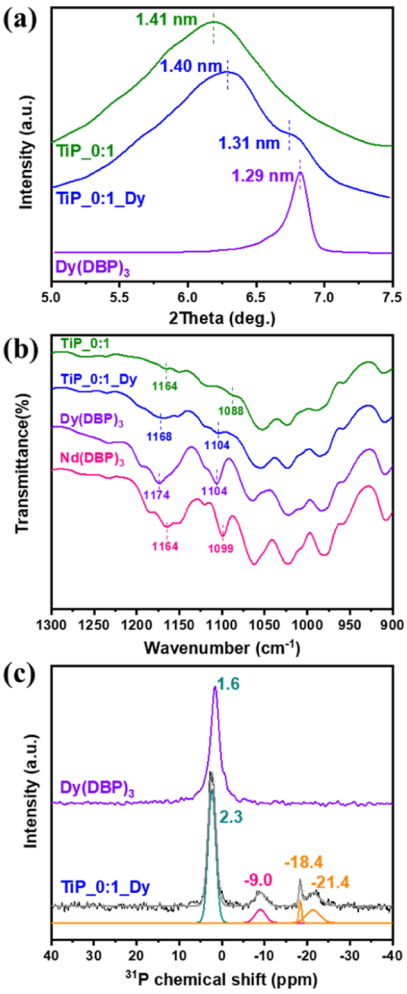

Figure 5. Characterizations of Dy^{3+}-loaded TiP_0:1 (TiP_0:1_Dy) compared with the original TiP_0:1 and/or synthesized $Dy(DBP)_3$ and $Nd(DBP)_3$. (a) Powder XRD patterns in the 2θ range of 5.0–7.5°. (b) ATR–FTIR spectra in the 900–1300 cm^{-1} range. (c) Solid-state ^{31}P MAS NMR spectrum with peak deconvolutions.

Extraction from Dilute Ln^{3+} Mixtures. The ion-exchange uptake preference of Ln^{3+} on the TiP_0:1 material was tested

DOI: 10.1021/acsami.8b04480
ACS Appl. Mater. Interfaces 2018, 10, 22083–22093

under batch condition in a mixture consisting of 10 mg L^{-1} of all Ln^{3+} ions. Because of their chemical similarity, Sc^{3+} and Y^{3+} were also added to the mixture. The extraction appeared to be pH-dependent, and the increase of equilibrium pH increased the uptake (Figure 6a). The pH dependency can be explained

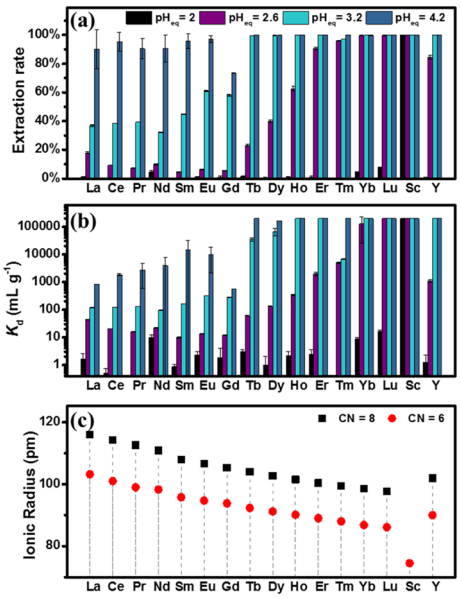

Figure 6. Extraction rates (a) and distribution coefficients (K_d) values (b) for metal uptake on the TiP_0:1 material. The ionic radii of the tested elements with different coordination numbers are indicated in (c).[3] Initial solution composition: 10 mg L^{-1} mixture of all Ln^{3+} (except radioactive Pm^{3+}) together with Sc^{3+} and Y^{3+}. The maximum K_d value in the study is presented as 199 800 mL g^{-1}, calculated from the detection limit (10 μg L^{-1}).

by eqs 5 and 6. Sc^{3+}, having the smallest ionic radius, was completely retained by the material even at pHs as low as 2.0. The extraction efficiency and K_d value for Y^{3+} lay between those for Ho^{3+} and Er^{3+}, and this is concurrent with their ionic radii for six-coordinated ions: 90.1 pm for Ho^{3+}, 90.0 pm for Y^{3+}, and 89.0 pm for Er^{3+}.

Across the Ln series, the extraction rate did not follow Ln contraction completely. Instead, the Ln "tetrad effect" was observed.[47] The extraction rate showed discontinuities at the positions of 1/4 filling (between Nd and Pm) and half filling (Gd) of the 4f electron subshell. The discontinuity at 3/4 filling (between Ho and Er) was not visible because of high extraction rates. This effect is commonly observed in the distribution of Ln in seawater and minerals, and it originates from the variations of interelectronic repulsion for the ground states across the Ln series.[48] In terms of the distribution coefficients (K_d, Figure 6b), a clear dividing line can be drawn between Gd and Tb. The present study establishes that the group separation between early Ln (La–Gd) and late Ln (Tb–Lu) could be effectively carried out on the TiP materials. The group SFs [SF(Tb–Lu/La–Gd)] were calculated as 2.0 ± 0.3, 28.7 ± 0.4, 203.1 ± 3.4, and 112.5 ± 35.3 at, respectively, pH 2.0, 2.6, 3.2, and 4.2.

Binary Ln^{3+} Separation Models. Binary Ln^{3+} uptake experiments were carried out to investigate in detail the potential separation behavior. Seven combinations were chosen across the Ln series: La–Ce, Pr–Nd, Eu–Gd, Gd–Tb, Tb–Dy, Yb–Lu, and Nd–Dy. The uptake of Ln^{3+} by the TiP_0:1 material from the 1 mM equimolar binary mixture was monitored as a function of solution equilibrium pH. Among these combinations, the first six represent adjacent Ln pairs, whereas the last one is a typical example for early and late Ln separation. The adjacent Ln pair Gd–Tb was studied because their distribution coefficients signify a clear discontinuity in the earlier section.

Adjacent Ln pairs are known to share extremely similar chemical properties, and their separation is one of the most difficult tasks in inorganic separations. The similarities of the adjacent Ln pairs are observed based on the almost identical shape of their K_d versus pH$_{eq}$ curves (in Figures S8–S13, Supporting Information). The uptake preference (represented by the SFs, Figure 7a–f) in the current case strictly followed

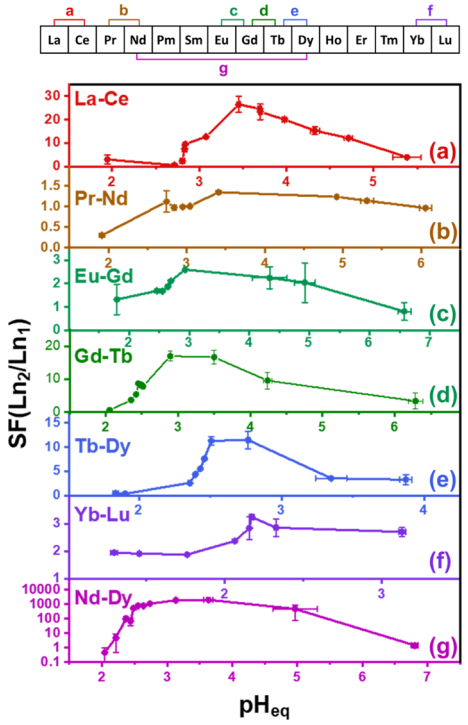

Figure 7. SFs between selected Ln^{3+} pairs [(a) La–Ce; (b) Pr–Nd; (c) Eu–Gd; (d) Gd–Tb; (e) Tb–Dy; (f) Yb–Lu; and (g) Nd–Dy] as a function of solution pH. Initial solution composition: 1 mM equimolar mixture of the selected Ln^{3+} pair. The corresponding K_d values are available in Figure S8–S14 in the Supporting Information.

the reversed Ln contraction order (Lu^{3+} → La^{3+}), whereby Ln^{3+} ions with smaller radii were preferentially retained. This deviates from the Ln tetrad effect. We suggest that the tetrad effect only becomes evident if the concentrations of Ln are relatively low. If there are large amounts of competing Ln^{3+} ions, the coordination and steric strain preferences favor the smaller Ln^{3+}. The separation between Gd and Tb is significantly easier compared to that between Eu and Gd, although both pairs are adjacent Ln. These results confirm the group separation behavior that Ln series is divided into two subgroups: from La to Gd as early Ln and from Tb to Lu as late Ln in our current work. In addition, significant Nd–Dy separation was achieved (Figures 7g and S14), possibly because of their larger differences in ionic radii.

The sole external parameter contributing to the separations is the equilibrium pH of the solution in our proposed system. This means that, through delicate control over the solution pH,

DOI: 10.1021/acsami.8b04480
ACS Appl. Mater. Interfaces 2018, 10, 22083–22093

optimal separations can be achieved either by leaving the majority of the larger Ln^{3+} in the solution or by exchanging the majority of the smaller Ln^{3+} onto the TiP material. The optimal molar fractions (best values obtained from the binary competitive batch systems) of the Ln in the liquid and solid phases are plotted in Figure 8a. Through only one uptake cycle, the heavier Ln in the adjacent Ln pairs was concentrated in the solid phase, representing some 60−80% of the total Ln fraction. Concurrently, the lighter Ln was concentrated in the liquid phase. The separation of Nd and Pr remained the most difficult one. Notably, almost complete Nd−Dy separation was achieved batchwise, as more than 99% of the loaded Ln was Dy.

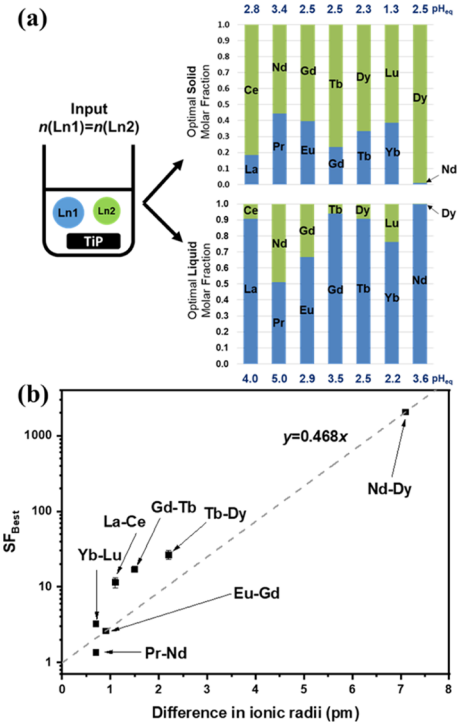

Figure 8. (a) Stacked column plots showing the optimal Ln fractions in the solid and the liquid phases obtained from the binary uptake study at different equilibrium pH values. (b) Dependence of the best achieved SFs using a logarithmic scale on the ionic radii difference of the Ln^{3+} pairs.

Because the separation capability originates from the small differences in ionic radii, we plotted the best achieved SFs (on a logarithmic scale) versus the differences in ionic radii (Figure 8b). Ln^{3+} forms an $Ln(DBP)_3$ complex; therefore, the ionic radii of six-coordinated ions were used. The linear regression line was drawn, and it appears that a larger difference in the ionic radii is positively correlated with the separation behavior. Overall, these results emphasize the potential technological significance of the TiP materials in Ln separation.

Transmetalation as a Metal Separation Process. Transmetalation is a type of organometallic reaction during which the organic ligands are transferred from one metal ion to another. It has been shown in recent years that MOFs and coordination polymers are applicable hosts for transmetalation. Partial, core−shell, complete, or even single-crystal-to-single-crystal metal exchanges were reported.[49] The metal exchange depends on ionic radii differences, preferential coordination geometries, kinetics, framework flexibility, and solvent effects.[50] It appears that transmetalation on water-stable MOFs and coordination polymers is worth exploring as a hydrometallurgical metal separation approach. The effects of codissolving metal ions (Fe^{3+}, Al^{3+}, Ca^{2+}, etc.) in real samples need to be taken into consideration when further assessing the performance of the process. However, the intralanthanide separation is still preferably to be placed as a downstream process when all other metal ions, except for Ln^{3+}, are eliminated.

Comparison with Literature Results. Table 4 summarizes some intralanthanide separation approaches reported in recent years, with an emphasis on solvent extraction,[51] solvent leaching,[52] crystallization,[8,15,26] and ion-exchange methods.[25,46] Organic phosphorus-containing ligands are in general selective for Ln separation. Our method appears to be the best in terms of SF, though this is far from the sole judgmental factor for a successful separation process. Titanium(IV) serves as sacrificial ion-exchange sites, and the dissolved TiO^{2+} hydrolyzes into hydroxides. In reality, the complete regeneration of the material might not be possible because of the formation of titanate phases. Additionally, organophosphates can be attacked by H^+, hydrolyzing into inorganic phosphate and alcohol. Finding a reasonable compromising point between selectivity and operational ease marks out our road ahead. The ultimate goal is a solvent-free, efficient, recyclable, and selective method that requires neither toxic chemicals nor intensive energy input.

Table 4. Intralanthanide Separation Capability Comparisons with Literature Reported Approaches

classification	method/reagent	target Ln pair	SF	references
solvent extraction	DEHPA	Nd−Dy	12.93	51
	Cyanex 923	Nd−Dy	12.79	51
solvent leaching	tripodal nitroxide ligand	Nd−Dy	359	52
crystallization	HDBP	Nd−Dy	>300	26
	borate	Nd−Dy	986	8
	camphorate	Tb−Dy	1.247	15
ion exchange	amorphous zirconium phosphate	Nd−Dy	1.9	25
	$Ce(DEHP)_3$	La−Dy	1.6	46
	$Fe(DEHP)_3$	La−Dy	18.4	46
	$Al(DEHP)_3$	La−Dy	3.5	46
	titanium(IV)butyl phosphate	Nd−Dy	2065	this work
		Tb−Dy	11.5	this work

CONCLUSIONS

We have demonstrated the basis of a Ln separation strategy utilizing a transmetalation reaction on layered titanium(IV) organophosphate materials, as opposed to the extraframework ion-exchange materials. These coordination polymers were easily prepared by a precipitation reaction and showed potential in intralanthanide separation, especially for the separation between early and late Ln. The selective Ln uptake was controlled by solution pH and did not require any additional energy input (e.g., hydrothermal condition). The selectivity arose from the ligand coordination and steric strain preferences during the transmetalation reaction and structural distortion. The separation performance of the transmetalation

DOI: 10.1021/acsami.8b04480
ACS Appl. Mater. Interfaces 2018, 10, 22083−22093

reaction seems higher compared to the selective crystallization or solvent extraction process utilizing the same or a similar organophosphate ligand. That said, the stability of the material as well as the regeneration needs to be further studied to warrant the design of a true separation process. Through alterations of the framework metal (size and valence) and organophosphate ligand, a variety of new MOF or coordination polymer materials can be envisioned with enhanced and tunable metal selectivity in aqueous solutions.

■ ASSOCIATED CONTENT

Supporting Information

The Supporting Information is available free of charge on the ACS Publications website at DOI: 10.1021/acsami.8b04480.

Formula calculation for TiPs, SEM images of the pyrophosphates, preliminary Ln uptake results, kinetic modeling, and K_d versus pH plots for binary Ln^{3+} extraction study (PDF)

■ AUTHOR INFORMATION

Corresponding Author

*E-mail: Wenzhong.Zhang@helsinki.fi.

ORCID

Wenzhong Zhang: 0000-0001-9184-0723
Sami Hietala: 0000-0003-1448-1813
Leonid Khriachtchev: 0000-0002-1146-5212
Timo Hatanpää: 0000-0003-3745-8296
Bhairavi Doshi: 0000-0002-8355-533X
Risto Koivula: 0000-0002-6547-9775

Notes

The authors declare no competing financial interest.

■ ACKNOWLEDGMENTS

The research leading to these results has received funding from the European Community's Horizon 2020 Program under grant agreement no. 636876 (MSCA-ETN REDMUD). This paper reflects only the authors' view, exempting the Community from any liability. Project website: http://etn.redmud.org/. W.Z. thanks Dženita Avdibegović (KU Leuven) for inspiring discussion and ICP-OES analysis and Karina Moslova (University of Helsinki) for CHN EA. The authors would like to dedicate this article in memoriam to Professor Risto Harjula (1956–2017), a pioneer in science, a beloved teacher, and a kind friend.

■ REFERENCES

(1) Bünzli, J.-C. G. Benefiting from the Unique Properties of Lanthanide Ions. *Acc. Chem. Res.* **2006**, *39*, 53–61.
(2) Binnemans, K. Lanthanide-Based Luminescent Hybrid Materials. *Chem. Rev.* **2009**, *109*, 4283–4374.
(3) Shannon, R. D. Revised Effective Ionic Radii and Systematic Studies of Interatomic Distances in Halides and Chalcogenides. *Acta Crystallogr., Sect. A: Cryst. Phys., Diffr., Theor. Gen. Crystallogr.* **1976**, *32*, 751–767.
(4) Kanazawa, Y.; Kamitani, M. Rare Earth Minerals and Resources in the World. *J. Alloys Compd.* **2006**, *408-412*, 1339–1343.
(5) Cotton, S. *Lanthanide and Actinide Chemistry*; John Wiley & Sons, 2013.
(6) Lucy, C. A. Evolution of Ion-Exchange: from Moses to the Manhattan Project to Modern Times. *J. Chromatogr. A* **2003**, *1000*, 711–724.
(7) Sun, X.; Luo, H.; Dai, S. Ionic Liquids-Based Extraction: A Promising Strategy for the Advanced Nuclear Fuel Cycle. *Chem. Rev.* **2011**, *112*, 2100–2128.
(8) Yin, X.; Wang, Y.; Bai, X.; Wang, Y.; Chen, L.; Xiao, C.; Diwu, J.; Du, S.; Chai, Z.; Albrecht-Schmitt, T. E.; Wang, S. Rare Earth Separations by Selective Borate Crystallization. *Nat. Commun.* **2017**, *8*, 14438.
(9) Hatanaka, T.; Matsugami, A.; Nonaka, T.; Takagi, H.; Hayashi, F.; Tani, T.; Ishida, N. Rationally Designed Mineralization for Selective Recovery of the Rare Earth Elements. *Nat. Commun.* **2017**, *8*, 15670.
(10) Tasaki-Handa, Y.; Abe, Y.; Ooi, K.; Narita, H.; Tanaka, M.; Wakisaka, A. Separation of Neodymium and Dysprosium by Forming Coordination Polymers. *Sep. Purif. Technol.* **2016**, *157*, 162–168.
(11) Gao, H. Y.; Peng, W. L.; Meng, P. P.; Feng, X. F.; Li, J. Q.; Wu, H. Q.; Yan, C. S.; Xiong, Y. Y.; Luo, F. Lanthanide Separation Using Size-Selective Crystallization of Ln-MOFs. *Chem. Commun.* **2017**, *53*, 5737–5739.
(12) Wang, Y.; Lu, H.; Dai, X.; Duan, T.; Bai, X.; Cai, Y.; Yin, X.; Chen, L.; Diwu, J.; Du, S.; Zhou, R.; Chai, Z.; Albrecht-Schmitt, T. E.; Liu, N.; Wang, S. Facile and Efficient Decontamination of Thorium from Rare Earths Based on Selective Selenite Crystallization. *Inorg. Chem.* **2018**, *57*, 1880–1887.
(13) Wang, Y.; Duan, T.; Weng, Z.; Ling, J.; Yin, X.; Chen, L.; Sheng, D.; Diwu, J.; Chai, Z.; Liu, N.; Wang, S. Mild Periodic Acid Flux and Hydrothermal Methods for the Synthesis of Crystalline f-Element-Bearing Iodate Compounds. *Inorg. Chem.* **2017**, *56*, 13041–13050.
(14) Li, X.-Z.; Zhou, L.-P.; Yan, L.-L.; Dong, Y.-M.; Bai, Z.-L.; Sun, X.-Q.; Diwu, J.; Wang, S.; Bünzli, J.-C.; Sun, Q.-F. A Supramolecular Lanthanide Separation Approach Based on Multivalent Cooperative Enhancement of Metal Ion Selectivity. *Nat. Commun.* **2018**, *9*, 547.
(15) Zhao, X.; Wong, M.; Mao, C.; Trieu, T. X.; Zhang, J.; Feng, P.; Bu, X. Size-Selective Crystallization of Homochiral Camphorate Metal-Organic Frameworks for Lanthanide Separation. *J. Am. Chem. Soc.* **2014**, *136*, 12572–12575.
(16) Florek, J.; Giret, S.; Juère, E.; Larivière, D.; Kleitz, F. Functionalization of Mesoporous Materials for Lanthanide and Actinide Extraction. *Dalton Trans.* **2016**, *45*, 14832–14854.
(17) Silbernagel, R.; Martin, C. H.; Clearfield, A. Zirconium(IV) Phosphonate-Phosphates as Efficient Ion-Exchange Materials. *Inorg. Chem.* **2016**, *55*, 1651–1656.
(18) Shusterman, J. A.; Mason, H. E.; Bowers, J.; Bruchet, A.; Uribe, E. C.; Kersting, A. B.; Nitsche, H. Development and Testing of Diglycolamide Functionalized Mesoporous Silica for Sorption of Trivalent Actinides and Lanthanides. *ACS Appl. Mater. Interfaces* **2015**, *7*, 20591–20599.
(19) Florek, J.; Chalifour, F.; Bilodeau, F.; Larivière, D.; Kleitz, F. Nanostructured Hybrid Materials for the Selective Recovery and Enrichment of Rare Earth Elements. *Adv. Funct. Mater.* **2014**, *24*, 2668–2676.
(20) Zheng, X.; Zhang, F.; Liu, E.; Xu, X.; Yan, Y. Efficient Recovery of Neodymium in Acidic System by Free-Standing Dual-Template Docking Oriented Ionic Imprinted Mesoporous Films. *ACS Appl. Mater. Interfaces* **2017**, *9*, 730–739.
(21) Zhang, W.; Avdibegović, D.; Koivula, R.; Hatanpää, T.; Hietala, S.; Regadío, M.; Binnemans, K.; Harjula, R. Titanium Alkylphosphate Functionalised Mesoporous Silica for Enhanced Uptake of Rare-Earth Ions. *J. Mater. Chem. A* **2017**, *5*, 23805–23814.
(22) Clearfield, A. Role of Ion Exchange in Solid-State Chemistry. *Chem. Rev.* **1988**, *88*, 125–148.
(23) Silbernagel, R.; Shehee, T. C.; Martin, C. H.; Hobbs, D. T.; Clearfield, A. Zr/Sn(IV) Phosphonates as Radiolytically Stable Ion-Exchange Materials. *Chem. Mater.* **2016**, *28*, 2254–2259.
(24) Zhang, W.; Koivula, R.; Wiikinkoski, E.; Xu, J.; Hietala, S.; Lehto, J.; Harjula, R. Efficient and Selective Recovery of Trace Scandium by Inorganic Titanium Phosphate Ion-Exchangers from Leachates of Waste Bauxite Residue. *ACS Sustainable Chem. Eng.* **2017**, *5*, 3103–3114.

DOI: 10.1021/acsami.8b04480
ACS Appl. Mater. Interfaces 2018, 10, 22083–22093

(25) Xu, J.; Koivula, R.; Zhang, W.; Wiikinkoski, E.; Hietala, S.; Harjula, R. Separation of Cobalt, Neodymium and Dysprosium Using Amorphous Zirconium Phosphate. *Hydrometallurgy* **2018**, *175*, 170−178.
(26) Tasaki-Handa, Y.; Abe, Y.; Ooi, K.; Narita, H.; Tanaka, M.; Wakisaka, A. Selective Crystallization of Phosphoester Coordination Polymer for the Separation of Neodymium and Dysprosium: A Thermodynamic Approach. *J. Phys. Chem. B* **2016**, *120*, 12730−12735.
(27) Tasaki-Handa, Y.; Abe, Y.; Ooi, K.; Narita, H.; Tanaka, M.; Wakisaka, A. Environmentally Friendly Separation of Dysprosium and Neodymium by Fractional Precipitation of Coordination Polymers. *RSC Adv.* **2014**, *4*, 20496−20498.
(28) Peppard, D. F.; Mason, G. W.; Maier, J. L.; Driscoll, W. J. Fractional Extraction of the Lanthanides as Their Di-Alkyl Orthophosphates. *J. Inorg. Nucl. Chem.* **1957**, *4*, 334−343.
(29) Tanaka, H.; Ishida, K.; Okumiya, T.; Murakami, M. Preparation and Exfoliation of Layered Titanium Butyl Phosphates. *Colloid Polym. Sci.* **2010**, *288*, 1427−1433.
(30) Ma, T.-Y.; Zhang, X.-J.; Shao, G.-S.; Cao, J.-L.; Yuan, Z.-Y. Ordered Macroporous Titanium Phosphonate Materials: Synthesis, Photocatalytic Activity, and Heavy Metal Ion Adsorption. *J. Phys. Chem. C* **2008**, *112*, 3090−3096.
(31) Zheng, T.; Yang, Z.; Gui, D.; Liu, Z.; Wang, X.; Dai, X.; Liu, S.; Zhang, L.; Gao, Y.; Chen, L.; Sheng, D.; Wang, Y.; Diwu, J.; Wang, J.; Zhou, R.; Chai, Z.; Albrecht-Schmitt, T. E.; Wang, S. Overcoming the Crystallization and Designability Issues in the Ultrastable Zirconium Phosphonate Framework System. *Nat. Commun.* **2017**, *8*, 15369.
(32) Assi, H.; Mouchaham, G.; Steunou, N.; Devic, T.; Serre, C. Titanium Coordination Compounds: From Discrete Metal Complexes to Metal-Organic Frameworks. *Chem. Soc. Rev.* **2017**, *46*, 3431−3452.
(33) Trublet, M.; Rusanova, D.; Antzutkin, O. N. Revisiting Syntheses of Ti(IV)/H_2PO_4-HPO_4 Functional Ion-Exchangers, Properties and Features. *New J. Chem.* **2018**, *42*, 838−845.
(34) Low, J. J.; Benin, A. I.; Jakubczak, P.; Abrahamian, J. F.; Faheem, S. A.; Willis, R. R. Virtual High Throughput Screening Confirmed Experimentally: Porous Coordination Polymer Hydration. *J. Am. Chem. Soc.* **2009**, *131*, 15834−15842.
(35) Gillens, A. R.; Powell, B. A. A Novel Technique for the Rapid Determination of Tributyl Phosphate Degradation From Alkaline Hydrolysis in Aqueous and Organic Phases Using FTIR-ATR and Verification of This Technique by Gas Chromatography. *J. Radioanal. Nucl. Chem.* **2016**, *307*, 1891−1899.
(36) Zhao, Y.; Zhu, G.; Jiao, X.; Liu, W.; Pang, W. Template Synthesis and Characterization of A New 2-D Layered Titanium Phosphate. *J. Mater. Chem.* **2000**, *10*, 463−467.
(37) Sakka, S.; Miyaji, F.; Fukumi, K. Structure of Binary K_2O−TiO_2 and Cs_2O−TiO_2 Glasses. *J. Non-Cryst. Solids* **1989**, *112*, 64−68.
(38) Schmutz, C.; Barboux, P.; Ribot, F.; Taulelle, F.; Verdaguer, M.; Fernandez-Lorenzo, C. EXAFS, Raman and 31P NMR study of amorphous titanium phosphates. *J. Non-Cryst. Solids* **1994**, *170*, 250−262.
(39) Thommes, M.; Kaneko, K.; Neimark, A. V.; Olivier, J. P.; Rodriguez-Reinoso, F.; Rouquerol, J.; Sing, K. S. W. Physisorption of Gases, With Special Reference to the Evaluation of Surface Area and Pore Size Distribution (IUPAC Technical Report). *Pure Appl. Chem.* **2015**, *87*, 1051.
(40) Yin, H.; Wada, Y.; Kitamura, T.; Kambe, S.; Murasawa, S.; Mori, H.; Sakata, T.; Yanagida, S. Hydrothermal Synthesis of Nanosized Anatase and Rutile TiO_2 Using Amorphous Phase TiO_2. *J. Mater. Chem.* **2001**, *11*, 1694−1703.
(41) Islam, F.; Rahman, H.; Ali, M. Solvent Extraction Separation Study of Ti(IV), Fe(III) and Fe(II) From Aqueous Solutions with Di-2-Ethyl Hexyl Phosphoric Acid in Benzene. *J. Inorg. Nucl. Chem.* **1979**, *41*, 217−221.
(42) Biswas, R. K.; Begum, D. A. Solvent Extraction of Tetravalent Titanium From Chloride Solution by Di-2-Ethylhexyl Phosphoric Acid in Kerosene. *Hydrometallurgy* **1998**, *49*, 263−274.
(43) Lumetta, G. J.; Sinkov, S. I.; Krause, J. A.; Sweet, L. E. Neodymium(III) Complexes of Dialkylphosphoric and Dialkylphosphonic Acids Relevant to Liquid-Liquid Extraction Systems. *Inorg. Chem.* **2016**, *55*, 1633−1641.
(44) Tasaki-Handa, Y.; Abe, Y.; Ooi, K.; Tanaka, M.; Wakisaka, A. Central Metal Ion Exchange in a Coordination Polymer Based on Lanthanide Ions and Di(2-Ethylhexyl)Phosphoric Acid: Exchange Rate and Tunable Affinity. *J. Colloid Interface Sci.* **2014**, *413*, 65−70.
(45) Tasaki-Handa, Y.; Abe, Y.; Ooi, K.; Tanaka, M.; Wakisaka, A. Steric Effect Involved in Ln^{3+}/Ce^{3+} Exchange in A Coordination Polymer Based on Di(2-Ethylhexyl)Phosphoric Acid. *Dalton Trans.* **2014**, *43*, 1791−1796.
(46) Ooi, K.; Tasaki-Handa, Y.; Abe, Y.; Wakisaka, A. Lanthanide Ion Exchange Properties of A Coordination Polymer Consisting of Di(2-Ethylhexyl) Phosphoric Acid and Trivalent Metal Ions (Ce^{3+}, Fe^{3+}, or Al^{3+}). *Dalton Trans.* **2014**, *43*, 4807−4812.
(47) Peppard, D. F.; Mason, G. W.; Lewey, S. A Tetrad Effect in the Liquid-Liquid Extraction Ordering of Lanthanides(III). *J. Inorg. Nucl. Chem.* **1969**, *31*, 2271−2272.
(48) Nugent, L. J. Theory of the Tetrad Effect in the Lanthanide-(III) and Actinide(III) Series. *J. Inorg. Nucl. Chem.* **1970**, *32*, 3485−3491.
(49) Das, S.; Kim, H.; Kim, K. Metathesis in Single Crystal: Complete and Reversible Exchange of Metal Ions Constituting the Frameworks of Metal−Organic Frameworks. *J. Am. Chem. Soc.* **2009**, *131*, 3814−3815.
(50) Lalonde, M.; Bury, W.; Karagiaridi, O.; Brown, Z.; Hupp, J. T.; Farha, O. K. Transmetalation: Routes to Metal Exchange Within Metal-Organic Frameworks. *J. Mater. Chem. A* **2013**, *1*, 5453−5468.
(51) Riaño, S.; Petranikova, M.; Onghena, B.; Vander Hoogerstraete, T.; Banerjee, D.; Foreman, M. R. S. J.; Ekberg, C.; Binnemans, K. Separation of Rare Earths and Other Valuable Metals From Deep-Eutectic Solvents: A New Alternative for the Recycling of Used NdFeB Magnets. *RSC Adv.* **2017**, *7*, 32100−32113.
(52) Bogart, J. A.; Lippincott, C. A.; Carroll, P. J.; Schelter, E. J. An Operationally Simple Method for Separating the Rare-Earth Elements Neodymium and Dysprosium. *Angew. Chem., Int. Ed.* **2015**, *54*, 8222−8225.

DOI: 10.1021/acsami.8b04480
ACS Appl. Mater. Interfaces 2018, 10, 22083−22093